Journal of Rock Mechanics and Geotechnical Engineering 16 (2024) 1348–1361

Contents lists available at ScienceDirect

Journal of Rock Mechanics and Geotechnical Engineering

journal homepage: www.jrmge.cn

Full Length Article

# Three-dimensional finite element simulation and reconstruction of jointed rock models using CT scanning and photogrammetry

Yingxian Lang [a], Zhengzhao Liang [a,*], Zhuo Dong [b]

[a] State Key Laboratory of Coastal and Offshore Engineering, Dalian University of Technology, Dalian, 116024, China
[b] School of Energy Science and Engineering, Henan Polytechnic University, Jiaozuo, 454003, China

ARTICLE INFO

*Article history:*
Received 19 February 2023
Received in revised form
3 May 2023
Accepted 14 August 2023
Available online 7 November 2023

*Keywords:*
X-ray computerized tomography (CT) scanning
Photogrammetry
Parallel computing
Numerical simulation
Uniaxial compression test
Digital image processing

ABSTRACT

The geometry of joints has a significant influence on the mechanical properties of rocks. To simplify the curved joint shapes in rocks, the joint shape is usually treated as straight lines or planes in most laboratory experiments and numerical simulations. In this study, the computerized tomography (CT) scanning and photogrammetry were employed to obtain the internal and surface joint structures of a limestone sample, respectively. To describe the joint geometry, the edge detection algorithms and a three-dimensional (3D) matrix mapping method were applied to reconstruct CT-based and photogrammetry-based jointed rock models. For comparison tests, the numerical uniaxial compression tests were conducted on an intact rock sample and a sample with a joint simplified to a plane using the parallel computing method. The results indicate that the mechanical characteristics and failure process of jointed rocks are significantly affected by the geometry of joints. The presence of joints reduces the uniaxial compressive strength (UCS), elastic modulus, and released acoustic emission (AE) energy of rocks by 37%–67%, 21%–24%, and 52%–90%, respectively. Compared to the simplified joint sample, the proposed photogrammetry-based numerical model makes the most of the limited geometry information of joints. The UCS, accumulative released AE energy, and elastic modulus of the photogrammetry-based sample were found to be very close to those of the CT-based sample. The UCS value of the simplified joint sample (i.e. 38.5 MPa) is much lower than that of the CT-based sample (i.e. 72.3 MPa). Additionally, the accumulative released AE energy observed in the simplified joint sample is 3.899 times lower than that observed in the CT-based sample. CT scanning provides a reliable means to visualize the joints in rocks, which can be used to verify the reliability of photogrammetry techniques. The application of the photogrammetry-based sample enables detailed analysis for estimating the mechanical properties of jointed rocks.



## 1. Introduction

As one of the most common geological structures, joints exist within almost all near-surface rocks (Xu et al., 2022) and significantly govern the mechanical properties of jointed rocks (Moomivand, 2014; Chang et al., 2019). The geometry of joints has a major influence on the failure modes and mechanical properties of rock masses in numerous engineering fields, including underground oil storage (Wang et al., 2020), underground excavation (Yang and Kulatilake, 2018), mining (Shen et al., 2021), rock slope stability (Haeri et al., 2015), and tunneling engineering. Therefore, detailed observation and characterization of joints are crucial for ensuring the safe construction of various rock engineering.

Rock joint measurement methods can be broadly classified into contact measurements and non-contact measurements. Contact measurements with measuring tools such as a compass, a magnifying glass, and a measuring tape, are a slow procedure and often cause large errors because a large proportion of joints cannot be measured (Fazio et al., 2019). Non-contact measurements, including terrestrial laser scanning and photogrammetry, can collect joint information without direct access to rock masses (Li et al., 2019). With advancements in digital image processing (DIP) and measurement techniques, the surveying process could greatly improve the measurement speed by extracting joint geometries from digital images (Wang et al., 2022), and thus the

* Corresponding author.
*E-mail address:* LiangZZ@dlut.edu.cn (Z. Liang).
Peer review under responsibility of Institute of Rock and Soil Mechanics, Chinese Academy of Sciences.

https://doi.org/10.1016/j.jrmge.2023.08.008

photogrammetry has been widely adopted (Salvini et al., 2020; Kong et al., 2021). Previous studies on joint photogrammetry have primarily focused on the extraction and estimation of a discontinuous parameter, such as orientation (Liu et al., 2022), persistence (Zhang et al., 2020), and frequency (He et al., 2017). However, the joints are simplified as lines or planes in numerous theoretical solutions such as damage constitutive law and fracture criterion, laboratory tests such as mechanical parameters and fracture evolution, and numerical simulations (Haeri et al., 2020; Zhang et al., 2020; Singh et al., 2022a, 2022b), without fully utilizing the collected joint information. Actually, joints within rocks typically develop in complex three-dimensional (3D) patterns, which are difficult to accurately represent in numerical simulations or theoretical analyses (Cotterell and Rice, 1980; Becker et al., 2001; Marji and Dehghani, 2010; Abdollahipour et al., 2016). Additionally, the accuracy of these measurements is unclear due to the lack of comprehensive comparisons with credible datasets, which limits their wider application (Kong et al., 2021). It is a key technical challenge to quantitatively and visually reveal the fracture evolution mechanism of irregular jointed rocks.

Natural joints have irregular shapes with rough surfaces (Yu et al., 2016; Aminpure and Moomivand, 2019), and the morphology of joints are quite different in terms of both shape and size, largely depending on the particular geological environment and type of rock. The roughness of rock joints significantly influences the mechanical behavior of rock masses (Guo and Qi, 2015). An accurate description of complex joint geometry is crucial, particularly for mechanical studies (Buyer et al., 2020). X-ray CT is a non-destructive method for analyzing the internal structures, such as joints in rocks, which provides a powerful tool for modeling the internal distribution of rock properties. Based on CT scans, the 3D numerical models can be constructed through DIP and 3D model reconstruction, which can reflect the mesostructures of rocks, such as pores (Lang et al., 2022) and mineral grains (Robinet et al., 2012). However, the rock sample size is limited by the CT detector size and the required resolution (Fig. 1), in which the resolution of a CT scanner is proportional to the size of the X-ray detector and inversely proportional to the size of the specimen (Elkhoury et al., 2019). The higher the resolution of the image is, the smaller the physical size of the specimen is, which means that the size of the specimen scanned by CT is limited. Therefore, CT scanning is not appropriate for field geological surveys or when the rock sample exceeds the size limit of CT scanners.

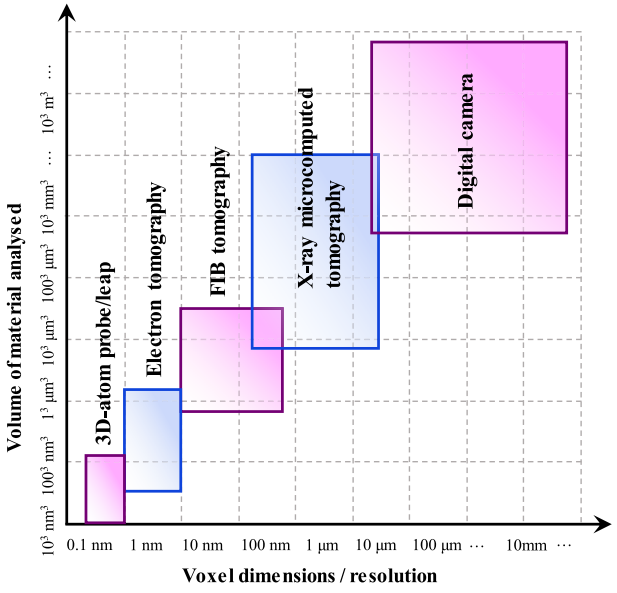


**Fig. 1.** Comparison of several imaging techniques, in which each technique has a specific range in terms of object size and resolution. Adapted from Madonna et al. (2012).

Compared with photogrammetry, the CT scanning is capable of obtaining detailed 3D joint information in rocks with less reliance on the post-processing of surveyors. Additionally, the characterization of joints is more precise and quantitative for CT scanning. Combining numerical simulations with DIP, the images reflecting the composition of rocks can be mapped into computer modeling systems to obtain the mechanical properties of rocks. Therefore, the CT scanning is effective to verify the reliability of photogrammetry techniques, which provides more detailed joint information in rocks and allows more precise and quantitative characterization of joints.

In this study, the spatial position and geometry of joints in a limestone sample were obtained by two methods, namely the X-ray CT scanning and photogrammetry. The method for establishing the digital joint model based on photogrammetry was proposed, and the cross-sectional images of the digital model were acquired. The CT images and cross-sectional images were integrated into RFPA$^{3D}$-digital, and the CT-based sample J1 and the photogrammetry-based sample J2 were respectively established. For comparative studies, the sample S1 without joints and the sample J3 with a joint simplified as a plane were constructed. The mechanical behaviors of these numerical samples were analyzed through parallel computing, including failure process, acoustic emission (AE) response characteristics, elastic modulus, and uniaxial compressive strength (UCS). Furthermore, the advantages and disadvantages of CT scanning and photogrammetry methods were compared and discussed, respectively. This study provides valuable insights into the critical roles of joints in rocks, and the CT-based sample J1 and photogrammetry-based sample J2 can be utilized to predict and estimate the mechanical characteristics of jointed rocks.

## 2. Brief description of RFPA$^{3D}$-digital

Developed based on RFPA$^{3D}$ (Liang et al., 2012), the RFPA$^{3D}$-digital combines DIP technology and parallel computing, and offers advantages in considering the mesoscopic and microscopic structures of rocks, which has been effectively used to investigate the impact of pores on the fracture evolution mechanisms of volcanic (Zhu et al., 2018) and basalt specimens (Lang et al., 2019a, 2019b, 2022), as well as the effects of joint spatial shape on the fracture process of rocks (Yu et al., 2016). Joint geometry information can be integrated into RFPA$^{3D}$-digital to investigate the mechanical properties of jointed rocks. In this study, the heterogeneity of rocks, the joints in rock mass and the damage localization are considered in the 3D numerical models. In this section, the governing equations of RFPA$^{3D}$-digital, and the implementation of DIP techniques in RFPA$^{3D}$-digital are introduced briefly.

### 2.1. Governing equations

Since rock is a heterogeneous material, the Weibull distribution is employed in RFPA$^{3D}$-digital to analyze the heterogeneous distribution of microstructures in rocks. The mechanical parameters of elements in numerical models constructed by RFPA$^{3D}$-digital are assumed to be disordered using Eq. (1) (Weibull, 1951):

$$f(\theta) = \frac{m}{\theta_0}\left(\frac{\theta}{\theta_0}\right)^{m-1} \exp\left[-\left(\frac{\theta}{\theta_0}\right)^{m}\right] \tag{1}$$

where $m$ represents a homogeneity index controlling the material homogeneity; $\theta$ represents mechanical parameters of elements, such as the UCS and elastic modulus; and $\theta_0$ is the mean value of mechanical parameters (Tang et al., 2001).

Fig. 2 illustrates the distribution probabilities of the elastic modulus with different homogeneity indexes, in which the $\theta_0$ is assumed as 10 GPa. The results clearly show that higher homogeneity index $m$ leads to greater probability for elements to reach $\theta_0$, resulting in more uniform mechanical responses in rocks. Conversely, when the homogeneity index is smaller, the basic mechanical parameters of rocks are more dispersed, resulting in a more discrete mechanical response.

In RFPA$^{3D}$-digital, the elements follow elastic-brittle constitutive laws in the damage process. Fig. 3a shows the elastic damage constitutive law for elements exposed to uniaxial tensile stress. Before the stress of the element reaches $\sigma_{c0}$, the elastic modulus of the element remains constant.

Rock is failed once the stress reaches $\sigma_{c0}$, and the elastic modulus progressively decreases with the development of damage. Therefore, according to elastic damage mechanics, the elastic modulus of damaged element is modified using Eq. (2):

$$E = (1 - D)E_0 \tag{2}$$

where $D$ represents the damage variable; $E$ and $E_0$ represent the elastic moduli of the damaged and intact elements, respectively.

When an element is in tension, it remains linear elasticity until the minimum principal stress reaches $\sigma_t$. If $\sigma_3 > \sigma_t$, the element strength falls to $\sigma_{tr}$, and the elastic modulus gradually decreases. When the tensile strain increases to $\varepsilon_{tu}$, the element loses its capability to load. The damage variable $D$ for elements under uniaxial tension is defined as below:

$$D = \begin{cases} 0 & (\bar{\varepsilon} > \varepsilon_{t0}) \\ 1 - \dfrac{\sigma_{tr}}{E_0\bar{\varepsilon}} & (\varepsilon_{tu} < \bar{\varepsilon} \le \varepsilon_{t0}) \\ 1 & (\bar{\varepsilon} \le \varepsilon_{tu}) \end{cases} \tag{3}$$

where $\sigma_{tr}$ denotes the residual strength of the element, and $\sigma_{tr} = -\lambda|\sigma_t|$, $\varepsilon_{t0}$ represents the tensile strain at the elastic limit (Fig. 3a). $\varepsilon_{tu}$ represents the element's ultimate tensile strain, which is defined as $\varepsilon_{tu} = \eta\varepsilon_{t0}$, where $\eta$ represents the ultimate strain factor.

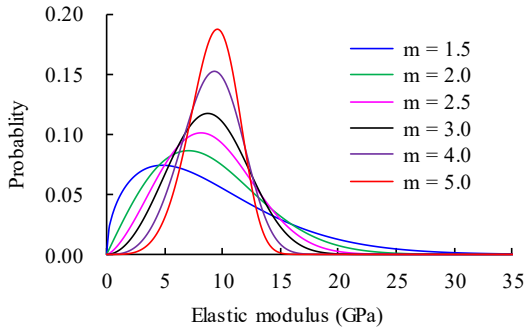


**Fig. 2.** Distribution probability of the elastic modulus of rocks with different homogeneity indexes.

The element equivalent principle tensile strain $\varepsilon$ is defined as below (Wang et al., 2006):

$$\bar{\varepsilon} = -\sqrt{\langle -\varepsilon_1\rangle^2 + \langle -\varepsilon_2\rangle^2 + \langle -\varepsilon_3\rangle^2} \tag{4}$$

where $\varepsilon_1$, $\varepsilon_2$, and $\varepsilon_3$ represent the maximum, minimum, and intermediate principal strains, respectively. The symbol "< >" is a mathematical operator defined as Eq. (5):

$$\langle x\rangle = \begin{cases} x & (x \ge 0) \\ 0 & (x < 0) \end{cases} \tag{5}$$

If the equivalent strain of an element is less than the ultimate tensile strain, the elastic modulus will be zero. To avoid ill-posed equations, the elastic modulus is set to $1.0 \times 10^{-5}$.

Fig. 3b illustrates the constitutive law for the element under compressive or shear stress. The damage variable $D$ for the element in shear failure mode is defined as below:

$$D = \begin{cases} 0 & (\bar{\varepsilon} < \varepsilon_{c0}) \\ 1 - \dfrac{\sigma_{rc}}{E_0\bar{\varepsilon}} & (\bar{\varepsilon} \ge \varepsilon_{c0}) \end{cases} \tag{6}$$

where $\sigma_{rc}$ represents the UCS of the element, $\sigma_{c0}$ represents the compressive stress of the element in shear damage state, as shown in Fig. 3b.

The elastic modulus of damaged elements subjected to different loading conditions can be calculated using Eq. (6) and Eq. (2). Subsequently, the calculation is restarted at the current loading and boundary conditions, and the stresses are redistributed until there is no new damage caused in the model. Then, the external load is increased and set as input for the following calculation step. This approach enables the simulation of the damage process of a numerical model under static loading conditions.

### 2.2. Implementation of DIP into RFPA$^{3D}$-digital

Rocks contain randomly distributed cracks, joints, and voids, and these pre-existing defects significantly affect the failure behaviors and mechanical characteristics of rocks. Digital images can reflect the microscopic structures of the materials through different color features.

Digital image processing technology uses computers to convert images into digital signals and processes them using algorithms, which has the functions of enhancing, restoring, segmenting images and extracting features, removing noise. In a grayscale image, an integer value can be used to represent the gray intensity of a pixel. In a true color image, pixels are represented by three integer values for the red, green, and blue levels. Thus, an image can be defined as Eq. (7) (Gonzalez and Woods, 2018):

$$h_k(x,y) = \begin{bmatrix} h(1,1) & h(1,2) & \cdots & h(1,Y) \\ h(2,1) & h(2,2) & \cdots & h(1,Y) \\ \vdots & \vdots & & \vdots \\ h(X,1) & h(X,1) & \cdots & h(X,Y) \end{bmatrix} \tag{7}$$

where $x$ ranges from 1 to $X$, $y$ ranges from 1 to $Y$, the variables $X$ and $Y$ represent the number of pixels in the vertical and horizontal directions, respectively. In the case of a grayscale image, $k$ equals 1, while for a true color image, $k$ takes values of 1, 2, and 3, respectively. Pixels in an image can be marked with individual labels determined by DIP techniques. Techniques such as noise reduction and image contrast enhancement can improve the visualization and analysis of microstructures.

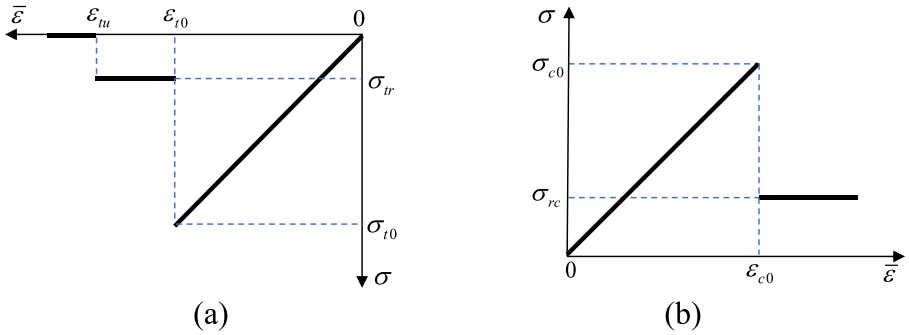


**Fig. 3.** Constitutive laws of (a) The element in tensile failure and (b) The element in shear failure (Liang et al., 2012).

The DIP techniques have been integrated into RFPA$^{3D}$ to create RFPA$^{3D}$-digital that can accurately characterize mesoscopic structures inside rocks by distinguishing the distinct color characteristics of different mineral types and structures. The mesh generation is conducted using RFPA$^{3D}$-digital and models are divided into small elements via the finite element method. An image of rock is composed of square pixels with the same size. Therefore, these pixels in a digital image can be mapped directly onto square elements in finite element mesh. By arranging and superimposing slice images of the rock sample in order, they can be mapped into 3D cuboid grids that represent the 3D microstructure of the rock sample. Different mechanical parameters can be assigned to various material elements according to the colors of pixels in sliced images, and then the 3D finite element rock model can be built by dividing rock materials. Although the basic governing formulae remain the same for all components (i.e. minerals) in models, the mechanical parameters differ for different materials.

The calculation flowchart of RFPA$^{3D}$-digital is shown in Fig. 4, which mainly consists of three parts, namely, the pre-processing, the finite element analysis, and the post-processing. The pre-processing phase includes functions such as the generation of 3D elements based on digital images, model setup, and material parameters assignment. The finite element analysis and post-processing phases include functions such as failure processing, result data generation, and 3D graphics creation.

When analyzing the fracture process of materials under static loading using RFPA$^{3D}$-digital, the external load is applied incrementally. At each step, an elastic finite element program is used to perform stress analysis, obtaining the stress field of all elements and the displacement field of nodes. Subsequently, the damage threshold criterion is utilized to determine if the element begins to be damaged. If the element is damaged in a particular loading step, the damage variable and elastic modulus of damaged element are calculated based on the elastic constitutive relationship. Considering the stress redistribution caused by element failure, it is necessary to recalculate the elastic matrix and final stiffness matrix under constant external load until no new element are damaged. The external load is then increased until the loading process is complete, and the deformation and fracture process of the numerical model can be obtained by this methodology.

### 2.3. Benchmark

To verify the effectiveness and reliability of RFPA$^{3D}$-digital, the numerical results are compared with physical tests of rock samples with different joint orientations, in which the experimental results are cited from Wasantha et al. (2012). The joint geometry (Fig. 5a), model dimensions, and boundary conditions were set based on the laboratory tests. Referring to Xu et al. (2013), the values of the elastic modulus, Poisson's ratio, and compressive strength for rock block elements were set to 56 GPa, 0.25, and 55 MPa, respectively. The values of elastic modulus, Poisson's ratio, and compressive strength for joint elements were set to 20 GPa, 0.2, and 5 MPa, respectively. Fig. 5 illustrates the experimental and numerical results of samples with different joint orientations. The variation of UCS with joint direction obtained from numerical simulation is consistent with experimental results (Fig. 5b). Fig. 5c and d presents failure patterns of the laboratory and numerical tests, respectively. The crack angle and position in the numerical tests closely match with those observed in the laboratory tests (Fig. 5d). Therefore, the experimental results are well matched with numerical simulation, indicating that RFPA$^{3D}$-digital is capable of simulating UC tests on jointed rocks.

## 3. Numerical model set-up

This study presents two techniques for integrating joints into numerical models. The first technique is based on CT scanning that was utilized to construct the CT-based sample J1, and the second technique is based on photogrammetry that was used to construct the photogrammetry-based sample J2. In addition to these two samples, intact sample S1, and sample J3 with a joint simplified as a plane, were constructed for contrast tests. It should be noted that all models have identical dimensions, element counts, and mechanical parameters.

### 3.1. CT-based sample

A limestone sample featuring natural joints, collected from Dalian, China, is presented in Fig. 9a. The sample exhibits a predominantly greyish-white appearance with irregular joints, and the size of the cylindrical rock specimen is 66 mm in diameter and 98 mm in height. The rock sample was scanned by μCT225kVFCB micro-CT experimental system at Taiyuan University of Technology, China, and a total of 1500 CT images (2048 × 2048 pixels) were acquired. The maximum magnification of the micro-CT system for the tested specimen can reach up to 400 times.

Like other imaging techniques, the CT imaging is susceptible to noise (Cnudde and Boone, 2013). To establish a reliable numerical model based on CT images, it is necessary to effectively preprocess the original CT images. In Fig. 6a, the noise is not obvious because the color of the rock matrix is similar to the noise color. However, significant amounts of noise become visible after the binarization process, as depicted in Fig. 6b. Hence, the CT images were median filtered to denoise. The median filter is a non-linear operation, commonly employed in image processing for noise removal. Fig. 6c illustrates the CT image after binarization and median filtering, indicating that median filtering yields satisfactory results in

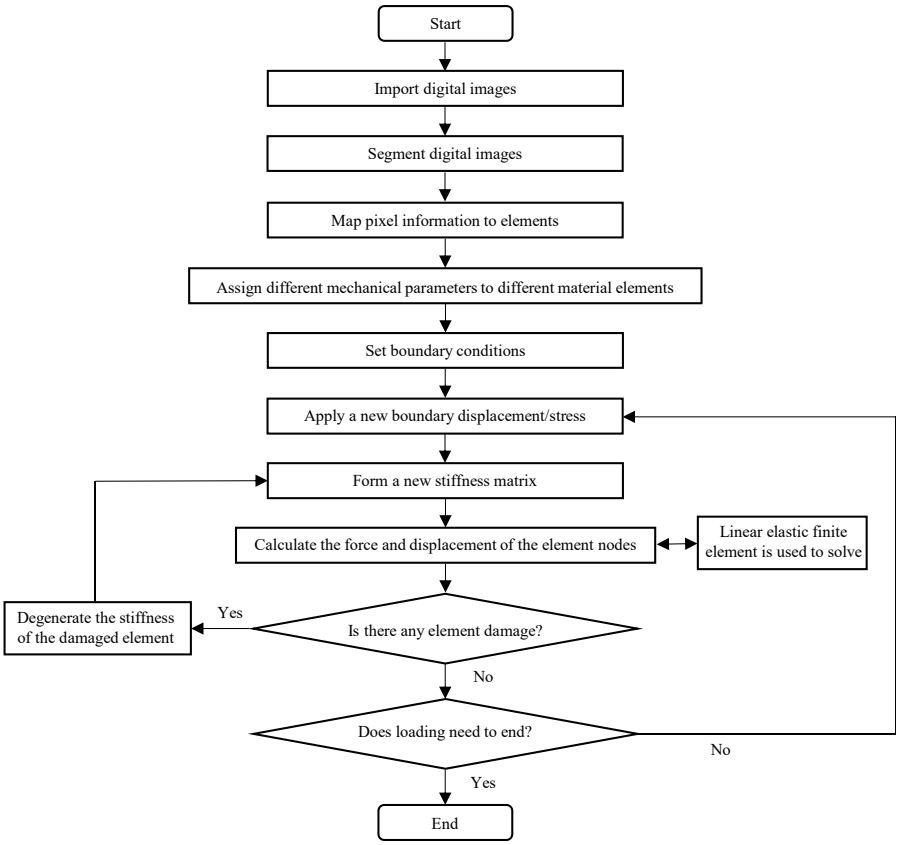


**Fig. 4.** Calculation flowchart of RFPA$^{3D}$-digital.

removing noise. Fig. 6d shows the grayscale value statistical chart of Fig. 6a. The grayscale value is obtained using Eq. (8):

$$I = (R+G+B)/3 \tag{8}$$

where $I$ represents the grayscale value; $R$, $G$, and $B$ are a sequence of three numbers, which represent the different contributions of red, green, and blue in determining the final color, respectively.

The value of grayscale $I$ in CT images represents the density of different rock materials. The grayscale value decreases as the density of the rock material decreases. It is worth noting that the grayscale of air is very low, typically falling within the range of 0–10. As shown in Fig. 6d, two peaks are observed, in which one represents the rock matrix and the other represents the air. The peak at the gray level equal to 0 represents the lower density which means the air, and the peak near the gray level equal to 200 represents higher density which means the rock matrix. It can be found from Fig. 6d that the gray threshold can be determined as 140, and thus the joints in the rock sample can be distinguished based on the threshold segmentation method.

Fig. 7 shows the basic principle of building a numerical model based on CT images and RFPA$^{3D}$-digital. In a two-dimensional (2D) image, each pixel is identifiable by its corresponding column number and row number, as shown in Fig. 7b. Each pixel is assigned a color, for instance, the pixel ($x_{03}$, $y_{03}$) has a gray value of 88. By threshold-based segmentation and region-based segmentation method, the target information can be extracted from the image (Fig. 7c), enabling the distinction and labeling of joint pixels and rock matrix pixels. The pixel coordinates of the images are then converted into spatial coordinates (Fig. 7d and e), and the information of each pixel is mapped to the finite element grid. Subsequently, a 3D numerical model is constructed by stacking these images in sequence (Fig. 7f).

CT scanning has been widely used in the field of geology to study the internal structure of rocks (Zhang et al., 2019), which has unique advantage to create high-resolution and accurate 3D models of rocks (Hampton et al., 2018; Fan et al., 2020; An et al., 2022). Researches have demonstrated that CT scanning is more precise to reflect the 3D mesostructural information inside the rocks compared to other traditional methods such as thin section analysis and manual drilling (Christe et al., 2011; Voorn et al., 2015). This is because CT scanning provides a detailed view of the internal structure of rocks, and thus many small fractures and fissures that may not be visible to the naked eye can be identified. Based on CT images, the joints can be accurately reconstructed in three dimensions. Therefore, the numerical model contains precise details of the joints, which is more conducive to obtaining accurate simulation results compared to the simplified joint model.

Although parallel computing is used, the computer capability is limited. Consequently, there exists an upper bound to the elements number that can be incorporated into a model, which ultimately results in a finite quantity of images and pixels available for constructing the model. In this study, a total of 123 CT images were selected at even intervals along the height direction of the sample. Additionally, the size of each CT image was reduced to dimensions of 100 × 100 pixels. The CT-based sample J1 is composed of 1.23 million elements with a diameter of 66 mm and a height of 98 mm, where each element is 0.66 mm × 0.66 mm × 0.8 mm in size. Table 1 shows the mechanical parameters of the sample J1, which have been calibrated to match the mechanical parameters of limestone referred to Al-Shayea (2004).

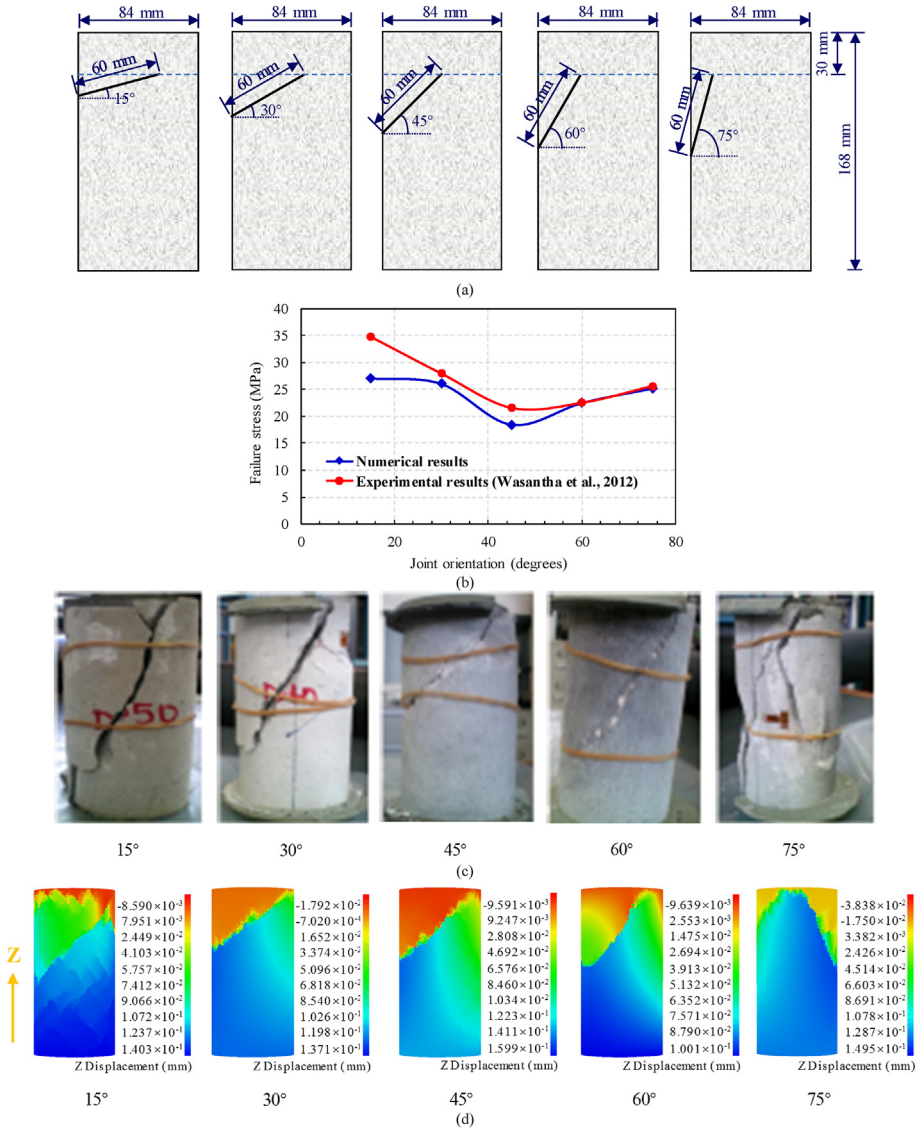


**Fig. 5.** Numerical and laboratory uniaxial compression test results for rock samples with different joint orientations: (a) Partially-spanning joint geometries; (b) Failure stress obtained by experiments (Wasantha et al., 2012) and simulations; (c) Failure patterns of laboratory test samples (Wasantha et al., 2012); and (d) Failure patterns of numerical samples.

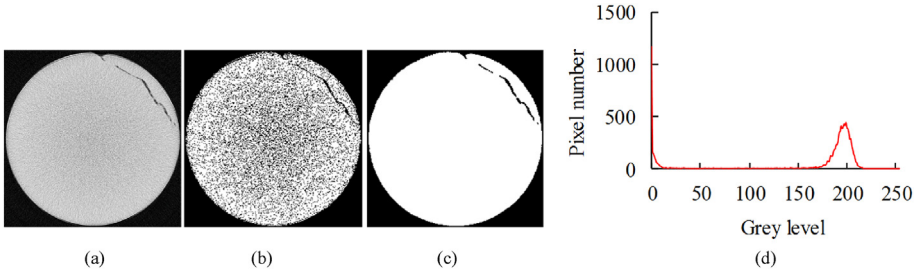


**Fig. 6.** CT image preprocessing: (a) CT image; (b) Image after binarization processing; (c) Image after binarization and median filtering processing; and (d) Grayscale value statistics of CT image.

### 3.2. Photogrammetry-based sample

Fig. 8 shows the workflow for constructing a jointed rock model using photogrammetric methods, which mainly consists of three parts, namely, the extraction of joint pixels, the transformation of joint coordinates, and the construction of a 3D jointed model based on joint point cloud data.

To construct the sample J2 based on photogrammetry, the joints on the surface of the limestone sample were photographed. A joint extraction program was developed based on the Sobel operator

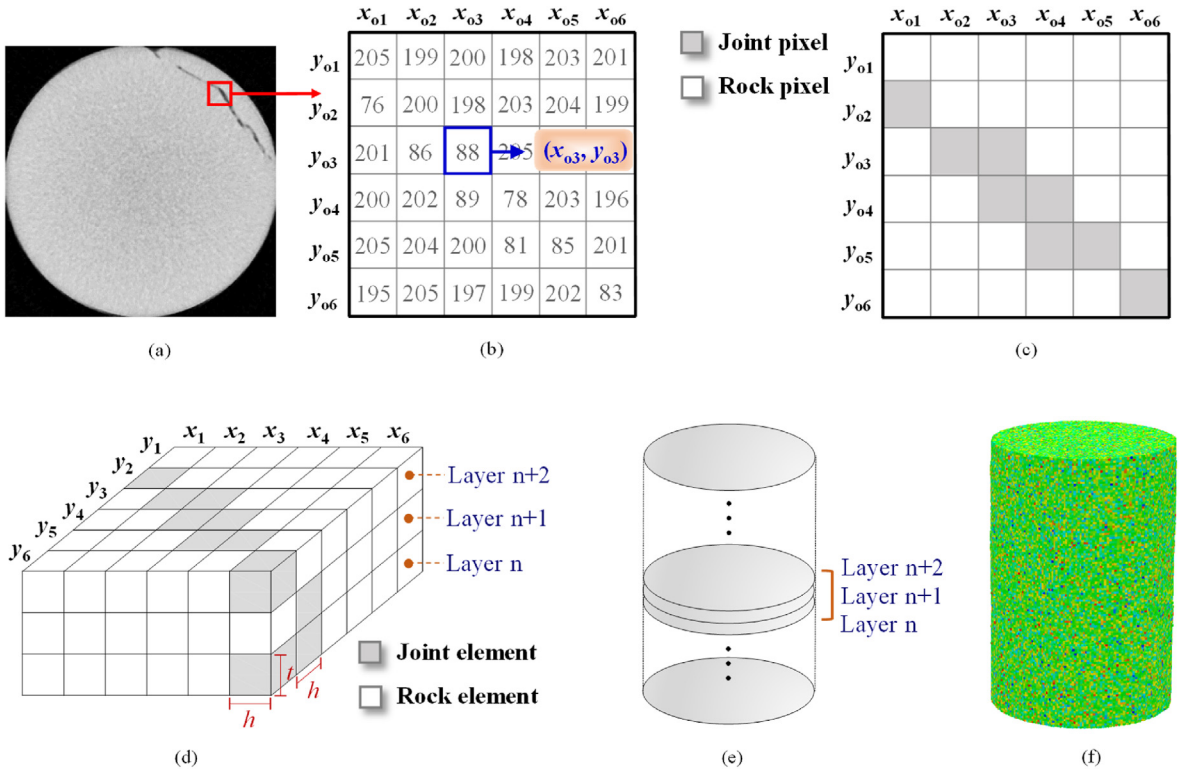


**Fig. 7.** Illustration of numerical model construction based on CT scanning: (a) CT image showing a joint trace; (b) 6-by-6 pixel grids, shown with gray values, row and column numbers; (c) Image segmentation; (d) Spatial coordinate system transformed from pixel coordinate; (e) Digital model constructed by stacking the images in sequence; and (f) CT-based sample J1.

(Gonzalez and Woods, 2018) while minimizing the degree of manual intervention in image processing. The extracted joint image is shown in Fig. 9b. By comparing the extracted joints with the original image, it was found that the extracted joint geometry information is consistent with the original joint geometry information, as shown in Fig. 9c.

To construct a digital model of jointed rock, the black pixels in Fig. 9b need to be converted to points in a 2D coordinate system, in which the DIP technology is used to map the pixel coordinates of the joints onto real 2D space coordinates (Fig. 9d). The coordinates data of joints were used to extend the 2D curve to a 3D joint surface, and then a joint digital model can be constructed (Fig. 9e). The digital model was sliced at equal intervals along the height direction, resulting in 123 slices that were used to construct the numerical sample J2 (Fig. 9f).

The material mechanical parameters for the sample J2 are presented in Table 1, which are identical to those for the sample J1. The sample J2 consists of 1.23 million elements, with each element size of 0.66 mm × 0.66 mm × 0.8 mm.

### 3.3. Intact sample and simplified joint sample

In addition to the CT-based sample J1 and the photogrammetry-based sample J2 described above, two additional samples were constructed, namely, the intact sample S1 without joints and the sample J3 with a joint simplified as a plane, in which the sample S1 was designed to investigate how joints might affect the mechanical properties of rocks. The sample J3 contains a joint, which was simplified according to the linear fitting of the joint as shown in Fig. 10. Joints are often simplified to straight lines or planes in experiments and numerical simulations. Therefore, the aim of constructing sample J3 is to obtain simulation results regardless of the curved joint geometry.

## 4. Results and discussion

To investigate the mechanical properties and failure process of four samples (i.e. J1, J2, J3, and S1), the UC tests were conducted by RFPA$^{3D}$-digital. The displacement load was applied to the top surface of each model, with a constant rate of 0.002 mm/step in the vertical direction.

### 4.1. Progressive failure process

Fig. 11 depicts the failure process of CT-based sample J1, represented in terms of vertical displacement distribution. It can be found that the displacement is uniformly distributed at the beginning of loading (Fig. 11a), and then discontinuous displacements occurs denoted by nonuniform colors around the joints as external displacement increases (Fig. 11b, c, and d). As shown in Fig. 11b, the stress concentration phenomena occur around the joints, and the initial cracks are formed along the joints. Cracks appear in the lower part of sample J1 and then propagate upward along the joints, forming a failure surface (Fig. 11c and d). Compared with the original joints in the rock sample (Fig. 9a), it can be found that the final damage region of sample J1 coincides with the surface joints of the limestone sample.

To better observe the effect of joints on the failure process, the sample J1 was sliced to observe the internal damage. Fig. 12 demonstrates the internal failure process of sample J1, in which the white part represents the joints and cracks. As depicted in Fig. 12a and b, the pre-existing joints are sources of crack formation, which determine the failure process and the final failure modes. As

**Table 1**
Mechanical parameters of the numerical models.

| Young's modulus (GPa) | Poisson's ratio | Frictional angle (°) | Compressive strength (MPa) | Tensile strength (MPa) |
|---|---|---|---|---|
| 50 | 0.35 | 30 | 230 | 23 |

external displacement increases, the cracks gradually propagate upward along the joints. It is worth noting that the cracks do not converge with the top left joint but extend all the way to the top of the sample (Fig. 12d). This observation indicates that the damage process is highly influenced by the spatial joint geometry.

The distribution and evolution of vertical displacement for the photogrammetry-based sample J2 are depicted in Fig. 13. It can be found that rock sample is initially damaged around the joints, resulting in an incompatible vertical displacement field. At the post-peak stage, uniform displacements appear in the upper block (shown in yellow in Fig. 13d), and a similar phenomenon is observed in the lower block of sample J2, resulting in the penetrating cracks along the joint surface. By comparing the surface cracks in Fig. 13d with pre-existing joints in Fig. 9e, it can be found that the cracks are affected by the curved surfaces of joints, indicating that joint geometry plays a significant role in the final failure pattern.

Fig. 14 shows the failure process of sample J2 in a vertical slice, in which the damage first occurs in the upper part of the joint during the initial stage of loading (Fig. 14a and b). As the external displacement increases, a new crack parallel to the Z-axis emerges at the end of the upper joint, as indicated by the circle mark in Fig. 14c. In the lower part of the sample, cracks propagate along with the pre-existing defects. It can be found in Fig. 14 that the cracks do not completely follow the pre-existing joints, mainly due to the influence of joint angle that have a vital influence on the deformation behavior under UC. Aminpure and Moomivand (2019) conducted uniaxial and triaxial compression tests on samples containing joints with different orientation angles, and found that joint orientation angles affect crack propagation direction. Haeri et al. (2020) studied the mechanical behavior of non-persistent joints with various orientation angles under compressive loading conditions, and found that the failure process is primarily determined by the number and angle of the joints. The damage patterns of jointed rocks are not only influenced by the geometry of joints, but also by the inclination of joints (Yang and Jing, 2010; Miao et al., 2018).

The fracturing process of jointed rock is significantly influenced by the spatial distribution of the joints. Damage primarily occurs in the weakest region of rocks due to the existence of joints. During initial loading, the damage zone is primarily generated at the joints under UC. The cracks tend to propagate along the direction of the joint. The failure surface of sample J1 is more irregular and curved than that of the sample J2. Additionally, the final damage region of sample J2 is not completely consistent with the joints shown in Fig. 9e. This is because the dip angle of joints will also affect the failure mode.

### 4.2. Stress-strain curves and stress analysis

The axial stress-strain curves of the four samples (i.e. J1, J2, J3, and S1) are presented in Fig. 15. The values of elastic modulus for the samples J1, J2, J3, and S1, are approximately 43.6 GPa, 44.1 GPa, 42.6 GPa, and 55.9 GPa, respectively. The UCS values for the samples J1, J2, J3, and S1, are approximately 72.3 MPa, 72.2 MPa, 38.5 MPa, and 115.72 MPa, respectively. As depicted in Fig. 15, the existence of joints in rock weakens the UCS and elastic modulus. Furthermore, the UCS and elastic modulus values of sample J2 are close to those of the sample J1, specifically the UCS of sample J2 is 1.001 times less than that of sample J1, and the elastic modulus of sample J2 is 1.011 times greater than that of sample J1. For the sample J3, the elastic modulus value is close to that of sample J1, which is 1.023 times less than that of sample J1. The UCS value of sample J3 is 1.878 times smaller than that of sample J1, indicating a significant difference between them. Therefore, the photogrammetry-based sample J2 demonstrates reliability in determining the UCS and elastic modulus of jointed rocks when compared to the sample J3.

Fig. 16 depicts the distribution of minimum principal stress in cross-sections of the four numerical specimens. The cross-sections pass through the joints in samples J1-J3. As shown in Fig. 16a–c and e-g, there are tensile stress concentration zones in the areas surrounding joints under UC, which significantly affect the failure process. In the sample S1 (Fig. 16d and h), no tensile stress concentration zone is observed since there are no joints present. The tensile strength of most rocks is weaker than their compressive strength, typically ten times less than the latter (Sheorey, 1997). As a result, stress concentration phenomena caused by joints often lead to rock mass damage. Griffith theory (Griffith, 1921) states that the failure of brittle materials is primarily influenced by internal defects such as cracks. In the case of compression, the stress concentration occurs at the crack tip due to the existence of tiny cracks, leading to destruction. Laboratory experiments have also found tensile stress concentration at the tip of joints (Mughieda and Alzo'ubi, 2004; Lee and Jeon, 2011). The existence of joints affects

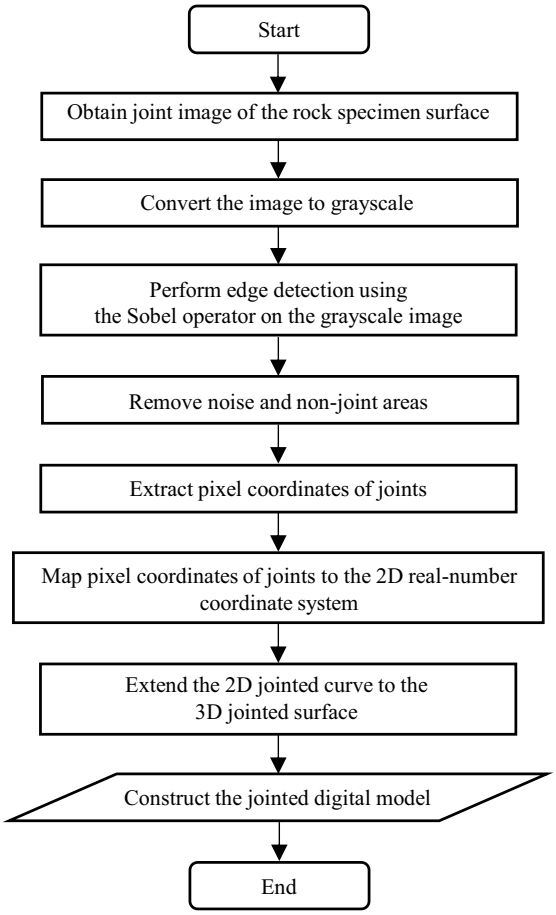


**Fig. 8.** Workflow of constructing digital joint model based on photogrammetry method.

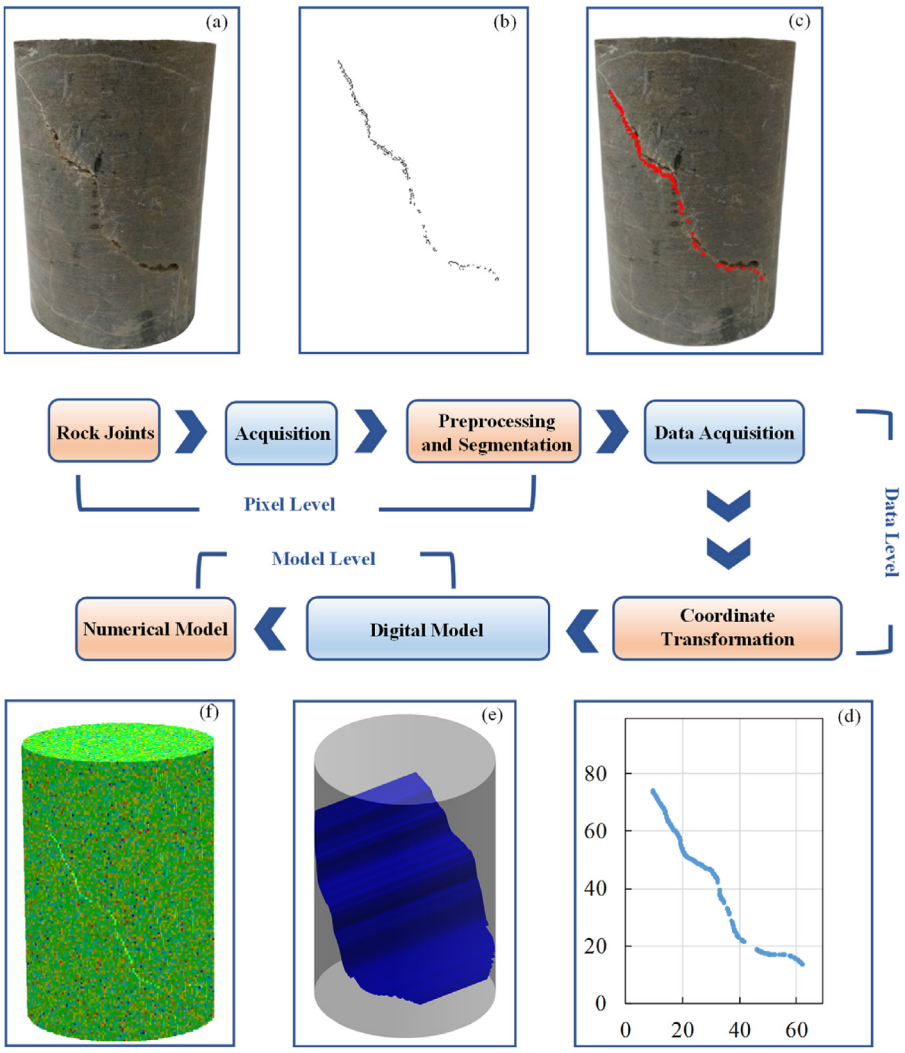


**Fig. 9.** Diagram of jointed rock numerical model construction system based on photogrammetry: (a) Rock surface image showing joints; (b) Extraction of joints; (c) Comparison of extracted joints and original photograph; (d) Coordinate points converted from joint pixels; (e) Digital model constructed by joint coordinate information; and (f) Numerical model built based on photogrammetry.

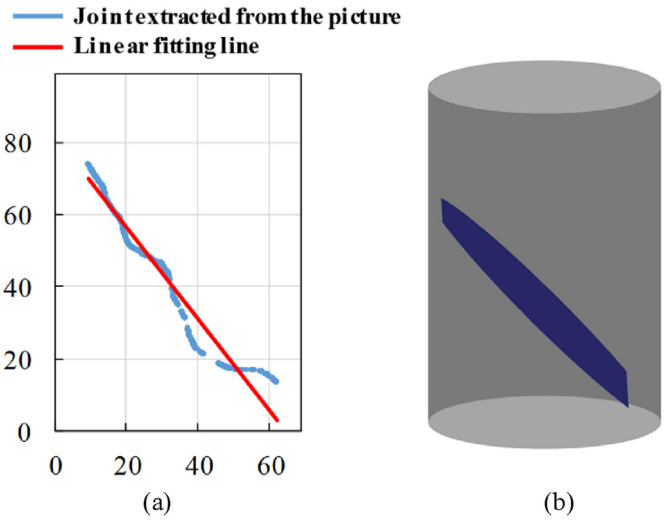


**Fig. 10.** Diagram of the joint in sample J3: (a) Joint coordinate diagram and (b) Digital model of sample J3.

the surrounding rock masses, making the embedded regions softer and weaker than intact rocks. Consequently, the mechanical properties of jointed rocks are different from that of intact rocks due to the influence of joints.

### 4.3. Acoustic emission response characteristics

Acoustic emission is a signal of damage in the rock samples. In RFPA$^{3D}$-digital, AE events are assumed to be produced by the damage in elements, which can be simulated by calculating the number of damaged elements and the AE energy released.

Fig. 17 depicts the accumulative released AE energy and AE counts under UC of the four samples (i.e. J1, J2, J3, and S1). It can be found that the AE characteristics of samples J1 and J2 are similar, and that the peaks of accumulative released AE energy in these two models are very close, which are 8204.11 J for the sample J1 and 7327.42 J for the sample J2. At the initial stage of loading, there are few AE counts and accumulative released AE energy for samples J1 and J2. With increasing displacement load, the AE counts and accumulative released AE energy gradually increase, and then reach their peak when samples J1 and J2 are seriously damaged. The peak accumulative released AE energy and AE counts for the intact

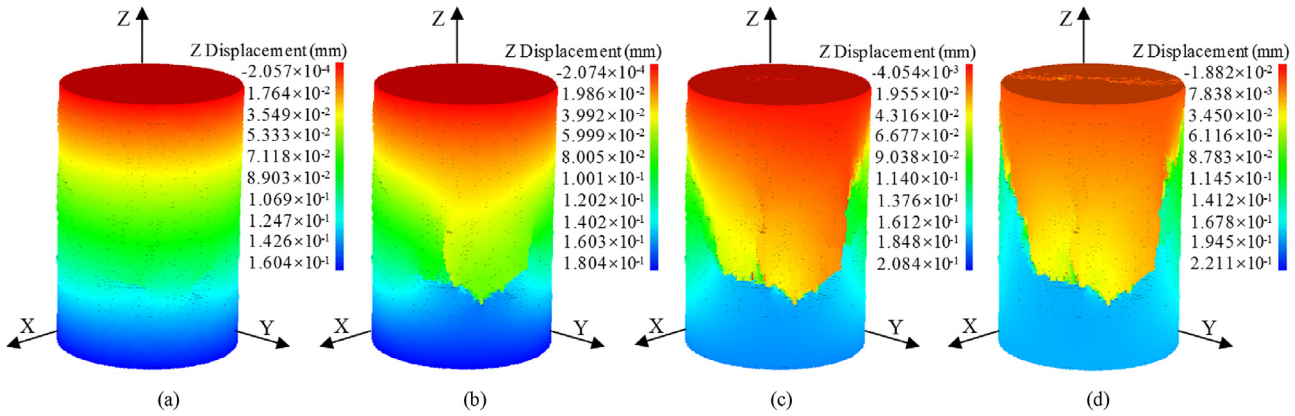


**Fig. 11.** Vertical displacement distribution and evolution of the CT-based sample J1: (a) 0.899$\varepsilon_p$; (b) 1.013$\varepsilon_p$; (c) 1.018$\varepsilon_p$; and (d) 1.019$\varepsilon_p$. $\varepsilon_p$ is the strain value corresponding to the peak stress.

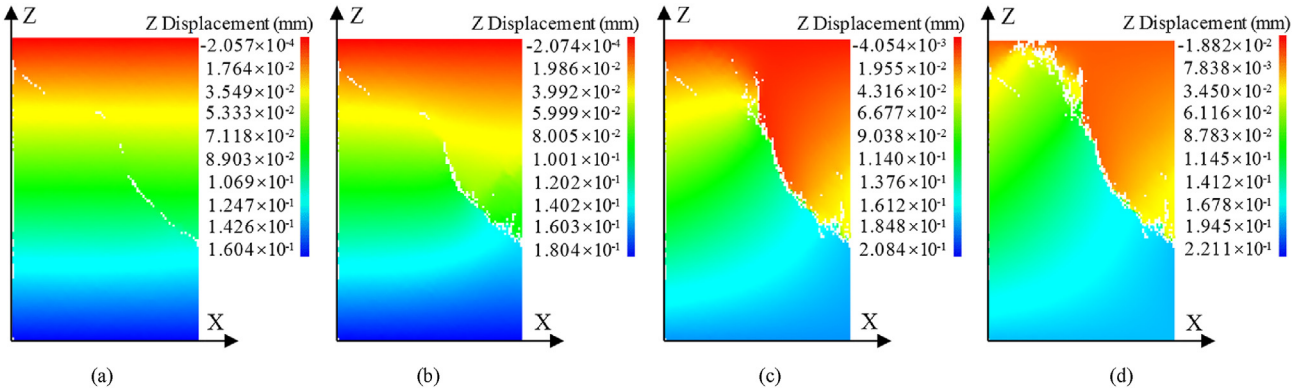


**Fig. 12.** Internal fracturing process of the CT-based sample J1 in a vertical slice: (a) 0.899$\varepsilon_p$; (b) 1.013$\varepsilon_p$; (c) 1.018$\varepsilon_p$; and (d) 1.019$\varepsilon_p$.

sample S1 are 17,339 J and 173,354, respectively, which is more than that of jointed rock samples J1, J2, and J3. The peak accumulative released AE energy values of samples J1, J2, and J3 are respectively 2.113, 2.366, and 9.857 times less than that of intact sample S1.

The AE evolution characteristics of samples J1 and J2 under UC are illustrated in Figs. 18 and 19, respectively, in which each sphere represents an AE event, and the red and blue represent the AE events caused by shear damage and tensile damage, respectively. It should be noted that some small-magnitude AE events were filtered out in Figs. 18 and 19. The AE signal provides valuable insights into the evolution process of damage inside the rock samples.

In the sample J1, AE events induced by shear and tensile damage primarily occur in the lower part of the sample (Fig. 18a). As displacement increases, cracks begin to form in the area of joints near the lower part of the sample (Fig. 11b). The cracks in sample J1 continue to propagate spatially along the natural shape of the joints (Fig. 18b and c). Concurrently, the upper part of the rock sample is also damaged, and the damage occurs both in the rock matrix and the joints.

For the sample J2, the AE events initially occur in the upper region of the sample (Fig. 19a), and then mainly occur around the joints with increasing load, and cracks are formed along the joints. The failure mode of sample J2 is mainly shear failure, which is also accompanied by tensile failure. As shown in Figs. 18d and 19d, the failure surface of sample J2 is flatter than that of sample J1.

As can be seen from Figs. 18 and 19, the shear failure dominates the failure mechanism of samples J1 and J2, with accompanying tensile failure. The evolution characteristics of AE events in samples J1 and J2 are different due to the variances in joint distribution, indicating that the 3D shapes of joints significantly affect the damage process. Notably, since the CT imaging provides a precise representation of joint distribution within rock samples, the fracture surface of sample J1 exhibits greater curvature and irregularity in comparison to that of the sample J2.

Although the failure surfaces formed in the samples J1 and J2 exhibit distinct differences, the accumulative released AE energy and AE counts in these two specimens are quite similar. For the sample J3, the AE results are quite different from that of samples J1 and J2. The AE energy in sample J3 is 4.663 and 4.165 times less than that of samples J1 and J2, respectively. Furthermore, the AE counts of samples J1 and J2 are 3.899 and 2.955 times greater than that of the sample J3, respectively. In addition, the UCS and elastic modulus values of sample J2 are close to those of sample J1. The sample J2 makes full use of the limited joint information on rock surfaces when the joint distribution in rocks cannot be obtained. Although there are some differences of joint geometry between the sample J2 and sample J1, the sample J2 can consider the trace length, persistence, and inclination of the joints. Nevertheless, the sample J3 simplifies the joints into a continuous surface, neglecting the persistence of the joints. Therefore, the accumulative released AE energy, AE counts, UCS, and elastic modulus of sample J3 are less than those of samples J1 and J2. According to the above analysis, the photogrammetry and DIP technologies can serve as viable alternatives for acquiring the characteristic information of joints when CT scanning is not feasible. For example, situations where field rock

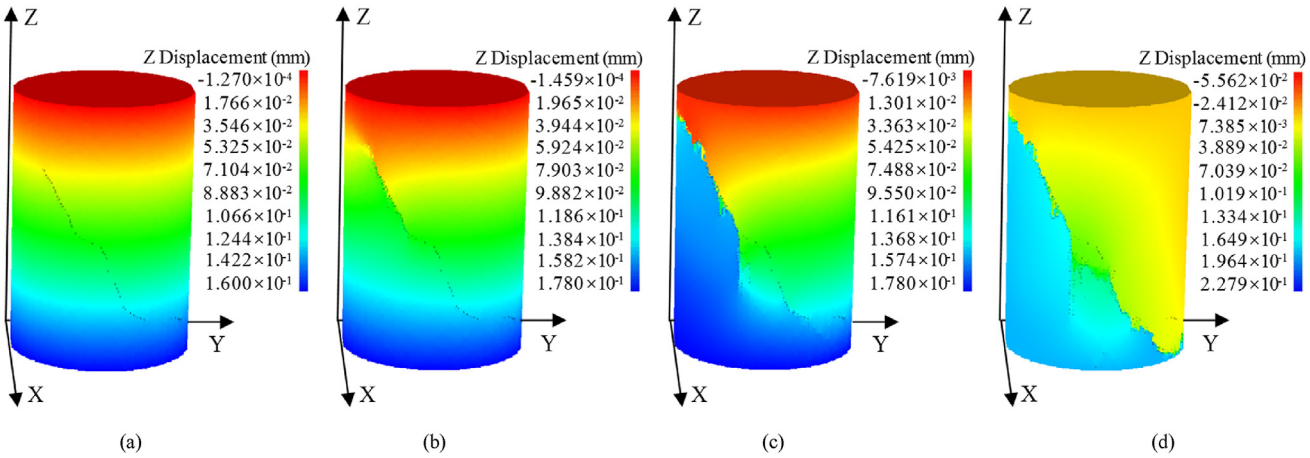


**Fig. 13.** Vertical displacement distribution and evolution of the photogrammetry-based sample J2: (a) 0.941$\varepsilon_p$; (b) 1.048$\varepsilon_p$; (c) 1.052$\varepsilon_p$; and (d) 1.057$\varepsilon_p$.

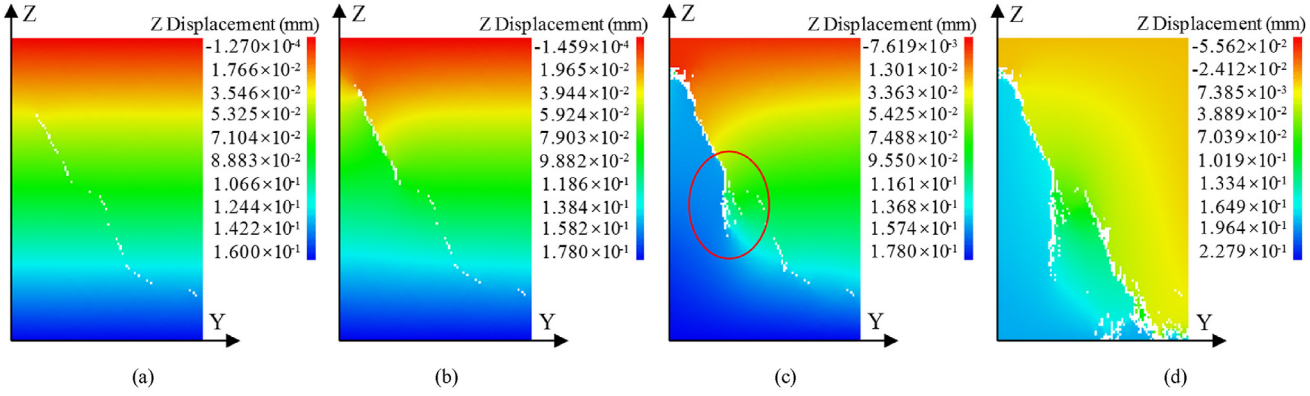


**Fig. 14.** Internal fracturing process of the photogrammetry-based sample J2 in a vertical slice: (a) 0.941$\varepsilon_p$; (b) 1.048$\varepsilon_p$; (c) 1.052$\varepsilon_p$; and (d) 1.057$\varepsilon_p$.

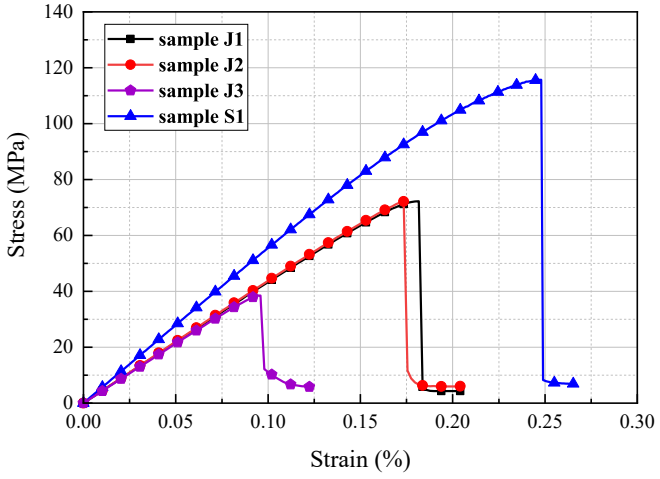


**Fig. 15.** Axial stress-strain curve of samples J1-J3, and S1 under uniaxial compression.

sampling is not feasible or the size of rock samples is excessive. The photogrammetry combined with DIP technologies can extract the joint information, including position, trace length, and inclination angle, which can be used for mechanical property evaluation and numerical simulation of jointed rocks.

By combining the photogrammetry, DIP technologies, and RFPA$^{3D}$-digital software, a novel method for constructing rock samples is proposed that closely mimic the real joint shape. This method makes full use of limited joint information on the rock surface when the distribution of internal rock joint information cannot be obtained. The photogrammetry-based sample can simulate the complex 3D shape of rock joints by generating a 3D joint surface from the 2D joint image. Since the authenticity, completeness, and representativeness of joint information are directly related to the value of the analysis results, it is essential to obtain joint information as accurately and comprehensively as possible. Precise joint information not only enhances the accuracy of scientific research, but also facilitates mathematical statistics of complex joint information. These statistics in turn promote the study of joint distribution patterns, rock mass structure, and rock mass mechanics.

## 5. Conclusions

Combining the CT scanning, photogrammetry, edge detection algorithms, and 3D matrix mapping methods, this study proposed approaches for constructing numerical models that considered the spatial geometry of joints. The joints were accurately mapped to the 3D numerical model (i.e. the sample J1) using CT scanning data. The sample J2 was constructed based on photogrammetry, and this modeling method is applicable to a wider range, allowing for the full utilization of the limited joint information on the rock surface.

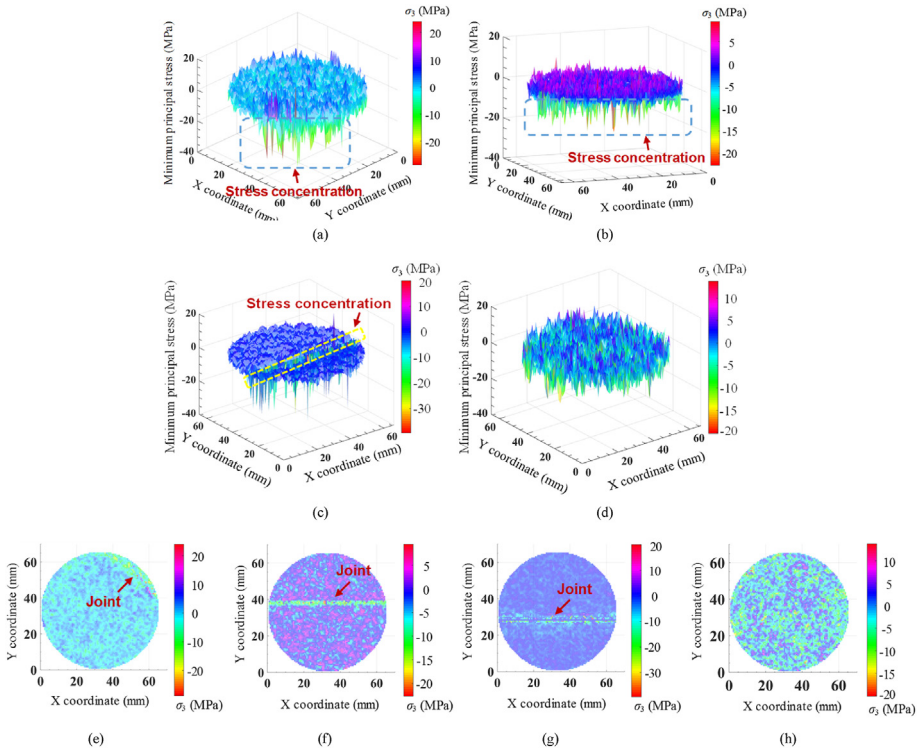


**Fig. 16.** 3D surface maps of minimum principal stress for (a) Cross-section 35 mm from bottom in CT-based sample J1, (b) Cross-section 29 mm from bottom in photogrammetry-based sample J2, (c) Cross-section 29 mm from bottom in simplified joint sample J3, (d) Cross-section 29 mm from bottom in intact sample S1, and (e ~ h) The corresponding 2D minimum principal stress maps.

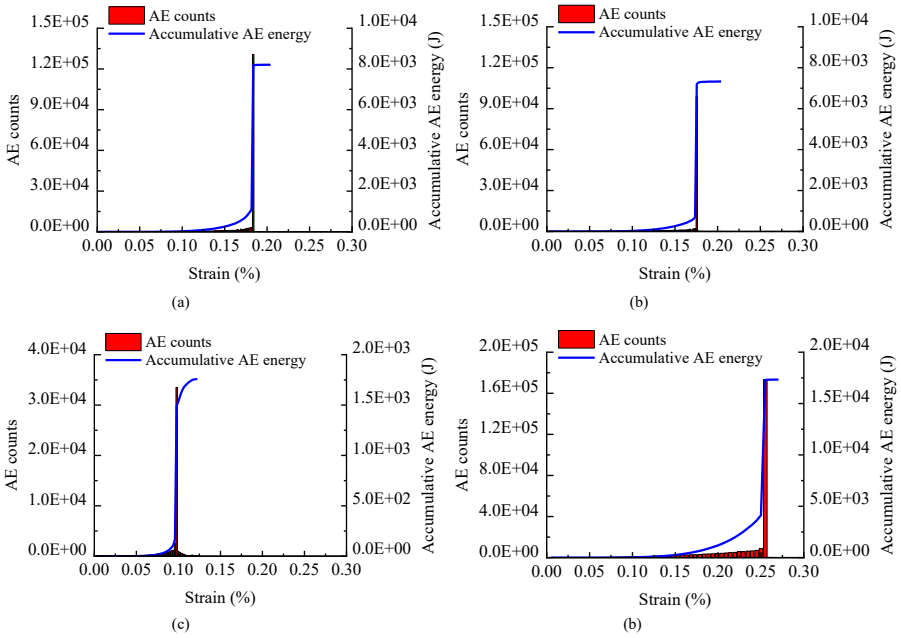


**Fig. 17.** AE response characteristics of samples (a) J1, (b) J2, (c) J3, and (d) S1 under uniaxial compression.

Additionally, an intact sample S1 without joints and a jointed rock specimen with the joint simplified into a plane (i.e. the sample J3) were constructed for comparative study. The mechanical properties and fracture process of the four samples (i.e. J1, J2, J3, and S1) under UC were numerically analyzed using parallel computing. The main conclusions are as follows.

(1) The simulation results indicate that the geometry of joints greatly affects the failure modes and stress field distribution

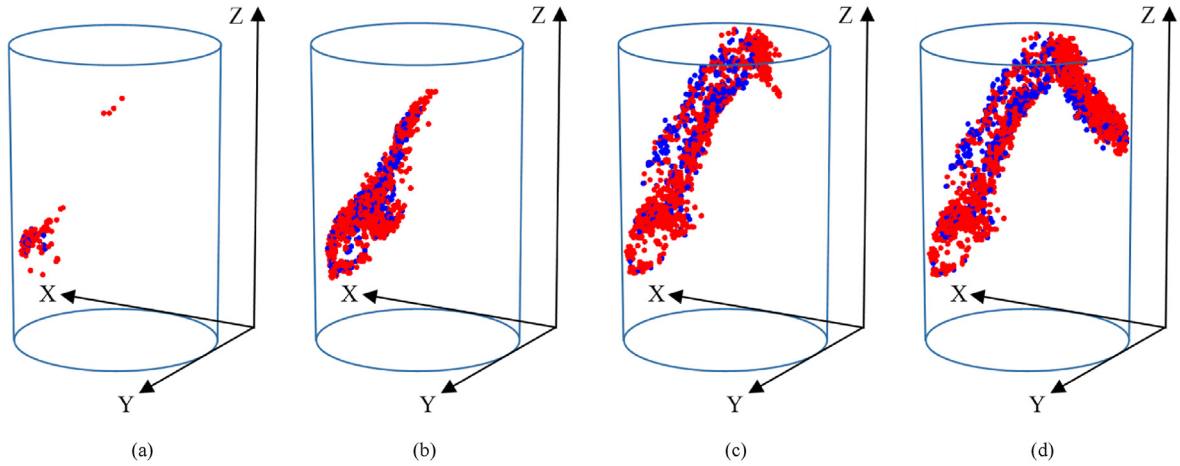


**Fig. 18.** Spatial distribution of AE events at different loading stages in the CT-based sample J1(a) 0.955$\varepsilon_p$, (b) 1.016$\varepsilon_p$, (c) 1.019$\varepsilon_p$, and (d) 1.023$\varepsilon_p$.

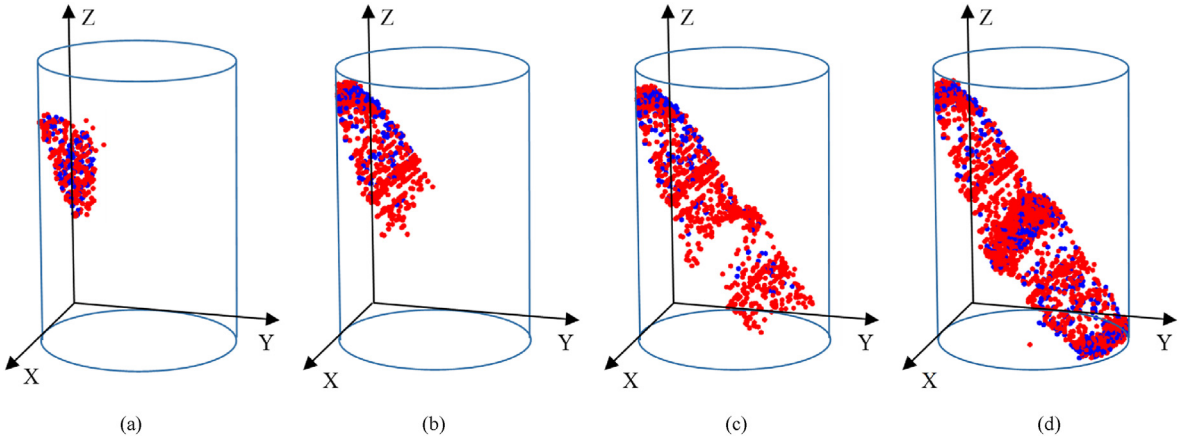


**Fig. 19.** Spatial distribution of AE events at different loading stages in the photogrammetry-based sample J2: (a) 1.04$\varepsilon_p$, (b) 1.051$\varepsilon_p$, (c) 1.054$\varepsilon_p$, and (d) 1.059$\varepsilon_p$.

of rocks. The presence of joints reduces the UCS, elastic modulus, and released AE energy of rocks by 37%–67%, 21%–24%, and 52%–90%, respectively. Additionally, the crack initiation and propagation around the joints are significantly influenced by the joint geometry and dip angle. The tensile stress concentration is observed around the caused damage and crack propagation from the tip of the joints, even under relatively small external loads.

(2) The locations of crack initiation and propagation vary for the joint samples J1, J2, and J3, due to the different internal joint geometry and structure. The UCS and elastic modulus values of the photogrammetry-based sample J2 are close to those of CT-based sample J1. In contrast, the UCS value (i.e. 38.5 MPa) of the simplified joint sample J3 is much lower than that of the sample J1 (i.e. 72.3 MPa). Compared to the simplified joint sample J3, the photogrammetry-based sample J2 makes full use of the available joint information, making it a reliable reference for predicting the UCS and elastic modulus of jointed rocks.

(3) Joints and their geometry are significant for evaluating and estimating the mechanical properties of jointed rocks. The CT scanning provides a reliable means to replicate and visualize joints in rocks, which can be used to verify the reliability of the photogrammetry techniques. Photogrammetry techniques, which makes full use of the limited joint geometry information, can provide more reliable results than methods that simplify joints to planes (or straight lines).

## Declaration of competing interest

The authors declare that they have no known competing financial interests or personal relationships that could have appeared to influence the work reported in this paper.

## Acknowledgments

This research was supported by the National Natural Science Foundation of China (Grant Nos. 42277150, 41977219), Henan Provincial Science and Technology Research Project (Grant No. 222102320271).

## References

Abdollahipour, A., Marji, M.F., Bafghi, A.Y., Gholamnejad, J., 2016. Time-dependent crack propagation in a poroelastic medium using a fully coupled hydromechanical displacement discontinuity method. Int. J. Fract. 199, 71–87.

Al-Shayea, N., 2004. Effects of testing methods and conditions on the elastic properties of limestone rock. Eng. Geol. 74 (1–2), 139–156.

Aminpure, F., Moomivand, H., 2019. Effect of discontinuity roughness and orientation on the parameters of the rock failure criterion under triaxial compressive stress. J. S. Afr. Inst. Min. Metall 119 (12), 1047–1060.

An, R., Kong, L., Zhang, X., Li, C., 2022. Effects of dry-wet cycles on three-dimensional pore structure and permeability characteristics of granite residual soil using X-ray micro computed tomography. J. Rock Mech. Geotech. Eng. 14 (3), 851–860.
Becker Jr., T.L., Cannon, R.M., Ritchie, R.O., 2001. Finite crack kinking and T-stresses in functionally graded materials. Int. J. Solid Struct. 38 (32–33), 5545–5563.
Buyer, A., Aichinger, S., Schubert, W., 2020. Applying photogrammetry and semi-automated joint mapping for rock mass characterization. Eng. Geol. 264, 105332.
Chang, L., Konietzky, H., Frühwirt, T., 2019. Strength anisotropy of rock with crossing joints: results of physical and numerical modeling with gypsum models. Rock Mech. Rock Eng. 52, 2293–2317.
Christe, P., Turberg, P., Labiouse, V., Meuli, R., Parriaux, A., 2011. An X-ray computed tomography-based index to characterize the quality of cataclastic carbonate rock samples. Eng. Geol. 117 (3–4), 180–188.
Cnudde, V., Boone, M.N., 2013. High-resolution X-ray computed tomography in geosciences: a review of the current technology and applications. Earth Sci. Rev. 123, 1–17.
Cotterell, B., Rice, J.R., 1980. Slightly curved or kinked cracks. Int. J. Fract. 16, 155–169.
Elkhoury, J.E., Shankar, R., Ramakrishnan, T.S., 2019. Resolution and Limitations of X-Ray Micro-CT with Applications to Sandstones and Limestones. Transp, vol. 129. Porous Media, pp. 413–425.
Fan, L., Gao, J., Du, X., Wu, Z., 2020. Spatial gradient distributions of thermal shock-induced damage to granite. J. Rock Mech. Geotech. Eng. 12 (5), 917–926.
Fazio, N.L., Perrotti, M., Andriani, G.F., Mancini, F., Rossi, P., Castagnetti, C., Lollino, P., 2019. A new methodological approach to assess the stability of discontinuous rocky cliffs using in-situ surveys supported by UAV-based techniques and 3-D finite element model: a case study. Eng. Geol. 260, 105205.
Gonzalez, R., Woods, R., 2018. Digital Image Processing, fourth ed. Pearson.
Griffith, A.A., 1921. The phenomena of rupture and flow in solids. Phil. Trans. Roy. Soc. Lond. 221, 163–198.
Guo, S., Qi, S., 2015. Numerical study on progressive failure of hard rock samples with an unfilled undulate joint. Eng. Geol. 193, 173–182.
Haeri, H., Khaloo, A., Marji, M.F., 2015. A coupled experimental and numerical simulation of rock slope joints behavior. Arabian J. Geosci. 8, 7297–7308.
Haeri, H., Sarfarazi, V., Ebneabbasi, P., Nazari maram, A., Shahbazian, A., Fatehi Marji, M., Mohamadi, A.R., 2020. XFEM and experimental simulation of failure mechanism of non-persistent joints in mortar under compression. Construct. Build. Mater. 236, 117500.
Hampton, J., Gutierrez, M., Matzar, L., Hu, D., Frash, L., 2018. Acoustic emission characterization of microcracking in laboratory-scale hydraulic fracturing tests. J. Rock Mech. Geotech. Eng. 10 (5), 805–817.
He, P., Li, S.C., Li, L.P., Zhang, Q.Q., Xu, F., Chen, Y.J., 2017. Discontinuous deformation analysis of super section tunnel surrounding rock stability based on joint distribution simulation. Comput. Geotech. 91, 218–229.
Kong, D., Saroglou, C., Wu, F., Sha, P., Li, B., 2021. Development and application of UAV-SfM photogrammetry for quantitative characterization of rock mass discontinuities. Int. J. Rock Mech. Min. Sci. 141.
Lang, Y., Liang, Z., Dong, Z., Wu, N., 2022. Mechanical behavior of porous rock based on the 3D digital image reconstruction and parallel computation. Environ. Earth Sci. 81 (18), 438.
Lang, Y.X., Liang, Z.Z., Dong, Z., 2019a. Three-dimensional microscopic model reconstruction of basalt and numerical direct tension tests. Chinese Journal of Engineering 41 (8), 997–1006 (in Chinese).
Lang, Y.X., Liang, Z.Z., Duan, D., Cao, Z.L., 2019b. Three-dimensional parallel numerical simulation of porous rocks based on CT technology and digital image processing. Rock Soil Mech. 40 (3), 1204–1212 (in Chinese).
Lee, H., Jeon, S., 2011. An experimental and numerical study of fracture coalescence in pre-cracked specimens under uniaxial compression. Int. J. Solid Struct. 48 (6), 979–999.
Li, X., Chen, Z., Chen, J., Zhu, H., 2019. Automatic characterization of rock mass discontinuities using 3D point clouds. Eng. Geol. 259, 105131.
Liang, Z.Z., Xing, H., Wang, S.Y., Williams, D.J., Tang, C.A., 2012. A three-dimensional numerical investigation of the fracture of rock specimens containing a pre-existing surface flaw. Comput. Geotech. 45, 19–33.
Liu, Y., Chen, J., Tan, C., Zhan, J., Song, S., Xu, W., Yan, J., Zhang, Y., Zhao, M., Wang, Q., 2022. Intelligent scanning for optimal rock discontinuity sets considering multiple parameters based on manifold learning combined with UAV photogrammetry. Eng. Geol. 309, 106851.
Madonna, C., Almqvist, B.S.G., Saenger, E.H., 2012. Digital rock physics: numerical prediction of pressure-dependent ultrasonic velocities using micro-CT imaging. Geophys. J. Int. 189 (3), 1475–1482.
Marji, M.F., Dehghani, I., 2010. Kinked crack analysis by a hybridized boundary element/boundary collocation method. Int. J. Solid Struct. 47 (7–8), 922–933.
Miao, S., Pan, P.Z., Wu, Z., Li, S., Zhao, S., 2018. Fracture analysis of sandstone with a single filled flaw under uniaxial compression. Eng. Fract. Mech. 204, 319–343.
Moomivand, H., 2014. Effects of orientation, frequency, and number of sets of discontinuities on rock strength under triaxial stresses. Arabian J. Geosci. 7 (12), 5345–5352.
Mughieda, O., Alzo'ubi, A., 2004. Fracture mechanisms of offset rock joints-A laboratory investigation. Geotech. Geol. Eng. 22, 545–562.
Robinet, J.C., Sardini, P., Coelho, D., Parneix, J.C., Prêt, D., Sammartino, S., Boller, E., Altmann, S., 2012. Effects of mineral distribution at mesoscopic scale on solute diffusion in a clay-rich rock: example of the Callovo-Oxfordian mudstone (Bure, France). Water Resour. Res. 48 (5).
Salvini, R., Vanneschi, C., Coggan, J.S., Mastrorocco, G., 2020. Evaluation of the use of UAV photogrammetry for rock discontinuity roughness characterization. Rock Mech. Rock Eng. 53, 3699–3720.
Shen, W., Shi, G., Wang, Y., Bai, J., Zhang, R., Wang, X., 2021. Tomography of the dynamic stress coefficient for stress wave prediction in sedimentary rock layer under the mining additional stress. Int. J. Min. Sci. Technol. 31 (4), 653–663.
Sheorey, P.R., 1997. Empirical Rock Failure Criteria. A.A. Balkema, Rotterdam.
Singh, J., Pradhan, S.P., Singh, M., Hruaikima, L., 2022a. Control of structural damage on the rock mass characteristics and its influence on the rock slope stability along National Highway-07, Garhwal Himalaya, India: an ensemble of discrete fracture network (DFN) and distinct element method (DEM). Bull. Eng. Geol. Environ. 81 (3), 96.
Singh, J., Pradhan, S.P., Singh, M., Yuan, B., 2022b. Modified block shape characterization method for classification of fractured rock: a python-based GUI tool. Comput. Geosci. 164, 105125.
Tang, C.A., Lin, P., Wong, R.H.C., Chau, K.T., 2001. Analysis of crack coalescence in rock-like materials containing three flaws-Part II: numerical approach. Int. J. Rock Mech. Min. Sci. 38 (7), 925–939.
Voorn, M., Exner, U., Barnhoorn, A., Baud, P., Reuschlé, T., 2015. Porosity, permeability and 3D fracture network characterisation of dolomite reservoir rock samples. J. Pet. Sci. Eng. 127, 270–285.
Wang, S.Y., Lam, K.C., Au, S.K., Tang, C.A., Zhu, W.C., Yang, T.H., 2006. Analytical and numerical study on the pillar rockbursts mechanism. Rock Mech. Rock Eng. 39, 445–467.
Wang, W., Zhao, W., Chai, B., Du, J., Tang, L., Yi, X., 2022. Discontinuity interpretation and identification of potential rockfalls for high-steep slopes based on UAV nap-of-the-object photogrammetry. Comput. Geosci. 166, 105191.
Wang, Z., Bi, L., Kwon, S., Qiao, L., Li, W., 2020. The effects of hydro-mechanical coupling in fractured rock mass on groundwater inflow into underground openings. Tunn. Undergr. Space Technol. 103, 103489.
Wasantha, P.L.P., Ranjith, P.G., Viete, D.R., Luo, L., 2012. Influence of the geometry of partially-spanning joints on the uniaxial compressive strength of rock. Int. J. Rock Mech. Min. Sci. 50, 140–146.
Weibull, W., 1951. A statistical distribution function of wide applicability. J. Appl. Mech. 18, 293–297.
Xu, C., Liu, Q., Wu, J., Deng, P., Liu, P., Zhang, H., 2022. Numerical study on P-wave propagation across the jointed rock masses by the combined finite-discrete element method. Comput. Geotech. 142, 104554.
Xu, T., Ranjith, P.G., Wasantha, P.L.P., Zhao, J., Tang, C.A., Zhu, W.C., 2013. Influence of the geometry of partially-spanning joints on mechanical properties of rock in uniaxial compression. Eng. Geol. 167, 134–147.
Yang, S.Q., Jing, H.W., 2010. Strength failure and crack coalescence behavior of brittle sandstone samples containing a single fissure under uniaxial compression. Int. J. Fract. 168, 227–250.
Yang, X.X., Kulatilake, P.H.S.W., 2018. Effect of joint micro mechanical parameters on a jointed rock block behavior adjacent to an underground excavation: a particle flow approach. Geotech. Geol. Eng. 37, 431–453.
Yu, Q.L., Yang, S.Q., Ranjith, P.G., Zhu, W.C., Yang, T.H., 2016. Numerical modeling of jointed rock under compressive loading using X-ray computerized tomography. Rock Mech. Rock Eng. 49, 877–891.
Zhang, P., Lee, Y.I., Zhang, J., 2019. A review of high-resolution X-ray computed tomography applied to petroleum geology and a case study. Micron 124, 102702.
Zhang, W., Lan, Z., Ma, Z., Tan, C., Que, J., Wang, F., Cao, C., 2020. Determination of statistical discontinuity persistence for a rock mass characterized by non-persistent fractures. Int. J. Rock Mech. Min. Sci. 126, 104177.
Zhu, J.B., Zhou, T., Liao, Z.Y., Sun, L., Li, X.B., Chen, R., 2018. Replication of internal defects and investigation of mechanical and fracture behaviour of rock using 3D printing and 3D numerical methods in combination with X-ray computerized tomography. Int. J. Rock Mech. Min. Sci. 106, 198–212.

**Dr. Zhengzhao Liang** is a professor at Dalian University of Technology and the dean of the Center for Rock Instability and Seismicity. His research interest includes rock fracture mechanics, numerical modeling of rock instability and failure, and stability analysis and monitoring of slopes and tunnels. Professor Liang won the Rocha Medal in 2008 and the Youth Science and Technology Award of CSRME. He hosted seven national research projects from the Ministry of Science and Technology of China and the Natural Science Fund of China. His research team has published more than 250 papers cited by more than 6200 times.